Research Article | Vol. 29, No. 18 / 30 Aug 2021 / Optics Express 28619
Optics EXPRESS

Actively tunable multi-band terahertz perfect absorber due to the hybrid strong coupling in the multilayer structure

KUN ZHANG,[1,2,3] FENG XIA,[1] SHIXIA LI,[1] YAN LIU,[1] AND WEIJIN KONG[1,4]

[1]College of Physics Science, Center for Marine Observation and Communications, Qingdao University, Qingdao 266071, China
[2]National Laboratory of Solid State Microstructures, Nanjing University, Nanjing 210093, China
[3]zkun@qdu.edu.cn
[4]kwjsd@163.com

Abstract: In this work, we propose a multi-band terahertz perfect absorber employing the topological photonic crystal combined with VO_2 and graphene. The hybrid strong coupling among the topological photonic state, the Tamm plasmon polaritons excited around the interfaces of VO_2 and graphene results in the three perfect absorption bands. Benefiting from the reversible insulator-metal phase transition of VO_2 and the tunable Fermi level of graphene, it can actively switch among no absorption, single-band, dual-band and multi-band absorptions around 1THz, with the absorption frequencies tunable as well. Besides, the absorption bands are sensitive to the incident angle in almost the same dispersion rate, with high absorptions in a large angle range. Moreover, the splitting frequencies between the adjacent absorption peaks strongly depend on the pair number of the alternating multilayers. Apart from the three absorption bands, there are still many absorption peaks in the large frequency range resulting from the standing waves, including other 7 peaks above 0.9 between 0.83THz and 1.55THz. Such a tunable multi-band absorber with multiple modulation methods may find extended applications in active integrated terahertz devices.

1. Introduction

Terahertz wave has attracted numerous attention due to the wide application prospects in spectroscopy and wireless communication [1,2]. However, few natural materials interact with THz radiation, resulting in the great demand for functional terahertz devices, such as switches, polarization converters and absorbers. Among them, perfect absorber with a near-unity absorption has become one of the most crucial components of sensors [3], modulators [4] cloaking [5] and imaging [6]. Benefitting from metamaterials [7,8], various terahertz perfect absorbers have been proposed, including narrow band [9,10], broadband [11–14], dual-band [15–19] and multi-band [20–22] absorbers. Multiband perfect absorbers have extensive applications in spectroscopic detection and phase imaging, as many kinds of drugs and explosives materials possess distinct fingerprints at multiple frequencies. General method to design dual- and multi-band terahertz perfect absorber is combing similar microstructures of different sizes horizontally or vertically, requiring precise microfabrication process to obtain the expected patterns. On the other hand, strong coupling system based on one-dimensional photonic crystals (PC) offers a convenient choice to design dual- and multi-band terahertz perfect absorbers [23–25], which is composed of alternating multilayers. The strong coupling systems support two or more optical modes with close frequencies, where the reversible energy exchange rate among them prevails their respective damping rates, giving rise to a set of splitting hybrid modes with perfect absorption. In these cases, the multiple absorption modes inherit the optical properties from those participating in the

#434714 https://doi.org/10.1364/OE.434714
Journal © 2021 Received 22 Jun 2021; revised 2 Aug 2021; accepted 11 Aug 2021; published 20 Aug 2021

Optics EXPRESS

strong coupling process, integrating the characteristics of every single mode into the resulted hybrid modes, which improves the diversity and tunability of the multi-band perfect absorbers.

In recent years, tunable perfect absorber gradually becomes a research focus due to the consideration of developing active terahertz devices. Employing tunable elements, such as photoconductive silicon [26], liquid crystal [27,28], graphene [29–32], Dirac semimetal [33] and VO_2 [34–36], the absorptance or the working frequency of the perfect absorbers can be actively controlled. Furthermore, bi-tunable perfect absorbers can be achieved by simultaneously taking the advantages of different active materials [37–39], enriching the modulation means and effects.

At the interface between one-dimensional PC and metal film, a unique electromagnetic surface state called Tamm plasmon polariton (TPP) can be excited [40], analogous to the electronic surface state predicted by Tamm [41]. On the other hand, the edge mode named topological photonic state (TPS) existing at the interface of a topological PC heterostructure is introduced by the analog between photonic systems and quantum systems [42,43], where the topological properties of the two semi-infinite systems on each side of the interface are different. In this work, we design a topological photonic crystal heterostructure combined with VO_2 and graphene, in which one TPS and two kinds of TPPs are excited. The strong coupling among the three modes leads to the multi-band terahertz perfect absorption with multiple modulation pathways. Both the absorption strength and the band number can be modulated because of the reversible insulator-metal phase transition of VO_2. The working frequencies and the bandwidths of the absorber can be controlled via the Fermi level of graphene. Besides, the working frequencies are sensitive to the incident angle as well. Moreover, there are also many high absorption peaks coming from the stand waves, expanding its potential applications in active terahertz switches, filters and detectors.

2. Structure design and simulation results

The hybrid topological photonic crystal heterostructure is shown in Fig. 1(a), consisting of VO_2, PC_1, PC_2 and monolayer graphene. The PC_1 is composed of 6 pairs of alternating silica and TPX films, while the PC_2 consists of 6 pairs of alternating silica and Zeonor films. In terahertz band, the TPX and Zeonor are low-loss polymers whose refractive indexes are $n_T = 1.46$ and $n_Z = 1.53$ [44], respectively, and the silica is also low-loss with the refractive index of $n_S = 1.95$ [45]. The film thicknesses in PC_1 and PC_2 are $d_{S1} = 40\mu m$, $d_T = 48\mu m$, $d_{S2} = 35\mu m$, $d_Z = 52\mu m$, respectively. The thickness of the silica spacer between PC_1 and VO_2 is $t_1 = 40\mu m$, and that between PC_2 and graphene is $t_2 = 28\mu m$. The thickness of VO_2 is $d_V = 30\mu m$.

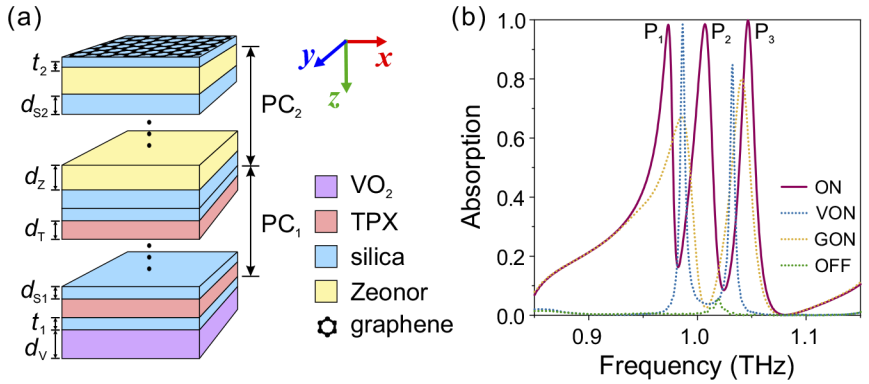

Fig. 1. (a) The schematic of the V/PC_1/PC_2/G structure. (b) The absorption spectra in the ON (solid line), VON (blue dotted line), GON (yellow dotted line) and OFF (green dotted line) states.

Optics EXPRESS

In this system, the absorption spectra can be modulated by tuning the Fermi level E_F of graphene and the conductivity σ_{VO2} of VO_2. We define the condition where $E_F = 0$ eV and $\sigma_{VO2} = 10$ S/m as the OFF state, $E_F = 0$ eV and $\sigma_{VO2} = 2\times10^5$ S/m as the VON state, $E_F = 0.7$ eV and $\sigma_{VO2} = 10$ S/m as the GON state, $E_F = 0.7$ eV and $\sigma_{VO2} = 2\times10^5$ S/m as the ON state. The absorption spectra in these states are shown in Fig. 1(b). In the OFF state, there is almost no absorption. In the VON and GON states, it behaves as a dual-band absorber. In the ON state, it acts as a multi-band perfect absorber, with three absorption peaks P_1, P_2 and P_3 at the frequencies of $f_1 = 0.97$ THz, $f_2 = 1.01$ THz and $f_3 = 1.05$ THz, respectively.

In simulation, the surface conductivity of graphene varies with the Fermi level E_F is expressed as [46]

$$\sigma_g \approx \frac{e^2 E_F}{\pi\hbar^2}\frac{i}{\omega + i\tau^{-1}}, \tag{1}$$

where τ is the carrier relaxation time following the equation $\tau = \mu E_F/(e{v_F}^2)$, depending on the carrier mobility $\mu = 1\times10^4$ cm^2/(V·s), the Fermi velocity $v_F = 1\times10^6$ m/s and the Fermi level. Consequently, the relative permittivity of graphene can be calculated by $\varepsilon_g = 1 + i\sigma_g/(\varepsilon_0\omega d_g)$ [47], in which the thickness of graphene is $d_g = 0.34$ nm. As shown in Fig. 2(a), the real part of the permittivity decreases to be negative as the Fermi level increasing, indicating that graphene turns to metallic medium. Apart from tuning the Fermi level for modulation, the E_F keeps 0.7 eV in the other conditions.

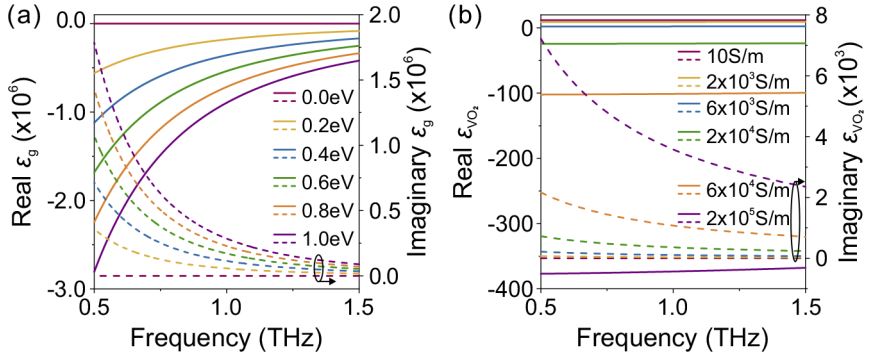

Fig. 2. The relative permittivity of (a) graphene and (b) VO_2, with the solid and dashed lines indicating the real and imaginary parts, respectively.

The relative permittivity of VO_2 in the terahertz band can be described by the Drude model as [48,49]

$$\varepsilon_{VO_2}(\omega) = \varepsilon_\infty - \frac{\omega_p^2(\sigma_{VO_2})}{\omega^2 + i\omega\gamma}, \tag{2}$$

where $\varepsilon_\infty = 12$, $\gamma = 5.75\times10^{13}$ rad/s, and the plasma frequency ω_p varying with the conductivity σ_{VO2}. It fits well with the experimental results when assuming the scattering rate remains constant in the phase transition temperature range and in the terahertz band [50]. In this condition, both σ and ${\omega_p}^2$ are proportional to the free carrier density, following [48]

$$\omega_p^2(\sigma_{VO_2}) = \frac{\sigma_{VO_2}}{\sigma_0}\omega_p^2(\sigma_0), \tag{3}$$

where σ_0 and $\omega_p(\sigma_0)$ are the conductivity of VO_2 and the corresponding plasma frequency at a certain temperature, respectively. By fitting the experimental results, when $\sigma_0 = 3\times10^5$ S/m, the corresponding plasma frequency $\omega_p(\sigma_0) = 1.4\times10^{15}$ rad/s [48]. The conductivity σ_{VO2} varies by five orders of magnitude in the reversible insulator-metal phase transition process, from 10 S/m

Optics EXPRESS

of the insulating state to 2×10^5 S/m of the metallic state [51]. As a result, the calculated relative permittivity of VO_2 are shown in Fig. 2(b). The real part of the permittivity becomes negative when σ_{VO2} is over 6×10^3 S/m, implying the transition from insulator to metal.

To explore the physical mechanism of the absorber, we calculate the spectra of the structures PC_1/PC_2, VO_2/PC_1 and PC_2/graphene, as shown in Fig. 3(a). The band structures of the single PC_1 and PC_2 can be obtained from [42]

$$\cos(q\Lambda) = \cos(k_a d_a)\cos(k_b d_b) - \frac{1}{2}\left(\frac{z_a}{z_b} + \frac{z_b}{z_a}\right)\sin(k_a d_a)\sin(k_b d_b), \tag{4}$$

in which $k_i = \omega n_i / c$, n_i and z_i are the refractive index and impedance of the slabs in PC ($i = a$ or b), q is the Bloch wave vector, d_a, d_b and $\Lambda = d_a + d_b$ are the thicknesses of the two slabs and the unit cell, respectively. As displayed in Fig. 3(b), the signs of the surface impedances in their common band gap around 1THz are opposite to each other, ensuring the emergence of the TPS. Besides, the density of state (DOS) of the PC_1/PC_2 structure in Fig. 3(b) reaches its maximum around 1THz, corresponding with the reflection dip in Fig. 3(a). Moreover, the electric field distribution at the frequency of the dip is shown in Fig. 3(c), where the field is mainly localized around the interface between PC_1 and PC_2. Therefore, the reflection dip for the PC_1/PC_2 structure comes from the excitation of TPS. There are absorption peaks around 1THz for both the VO_2/PC_1 and PC_2/graphene structures when $\sigma_{VO2} = 2\times10^5$ S/m and $E_F = 0.7$ eV, whose field distributions are given in Figs. 3(d) and 3(e), respectively. The field localizations

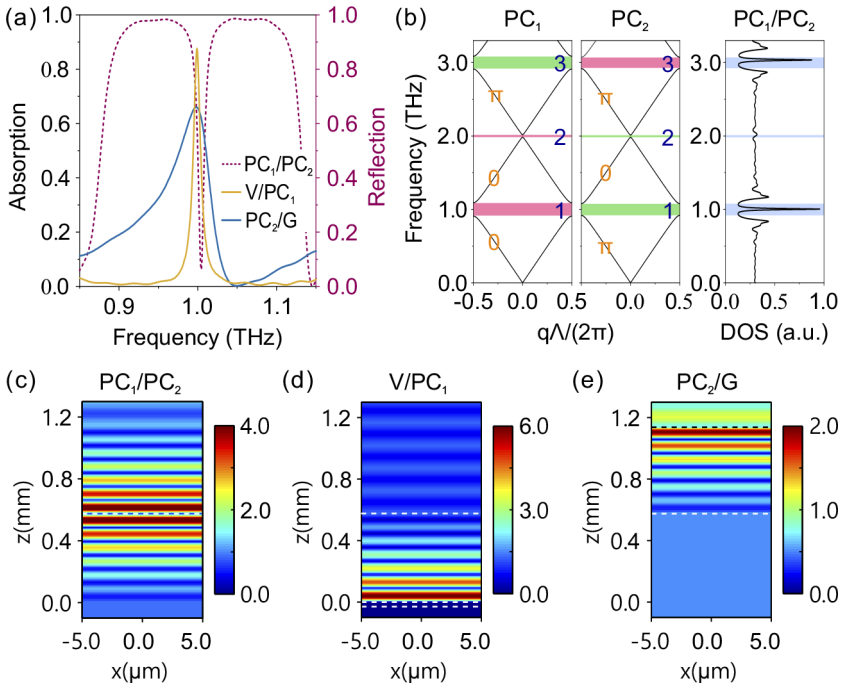

Fig. 3. (a) The reflection spectra of the PC_1/PC_2 (red dotted line), the absorption spectra of the V/PC_1 (yellow solid line) and PC_2/G (blue solid line) for VON and GON states, respectively. (b) Left and middle, the band structures of the PC_1 and PC_2, where the band gap and the Zak phase of every band are listed with blue and orange labels, respectively. Right, the DOS of the PC_1/PC_2 structure, where the blue shadows are in the same position with those indicating the band gaps in the band structures. (c)-(e) The electric field distributions at the frequencies of the dip and peaks in (a).

Optics EXPRESS

occur around the interfaces of VO_2/PC_1 and PC_2/graphene, indicating the existence of the Tamm plasmon polaritons because VO_2 and graphene both serve as metallic medium in these conditions. The corresponding modes are labelled as VTP and GTP, respectively. Therefore, three photonic modes, the TPS, VTP and GTP, can be excited in the VO_2/PC_1/PC_2/graphene structure in the ON state.

Furthermore, we calculate the field distributions at the absorption peaks P_1-P_3 of the ON state, as shown in Figs. 4(a)–4(c), where the fields are simultaneously localized around the boundaries of VO_2/PC_1, PC_1/PC_2 and PC_2/graphene. Thus, the multi-band absorptions come from the hybrid strong coupling among the TPS, VTP and GTP modes, as schematically described in Fig. 4(d). For the VON state, the dual-band absorption comes from the strong coupling of TPS and VTP, as the GTP cannot be excited. For the GON state, the strong coupling between TPS and GTP results in the dual-band absorption, because of the absence of VTP.

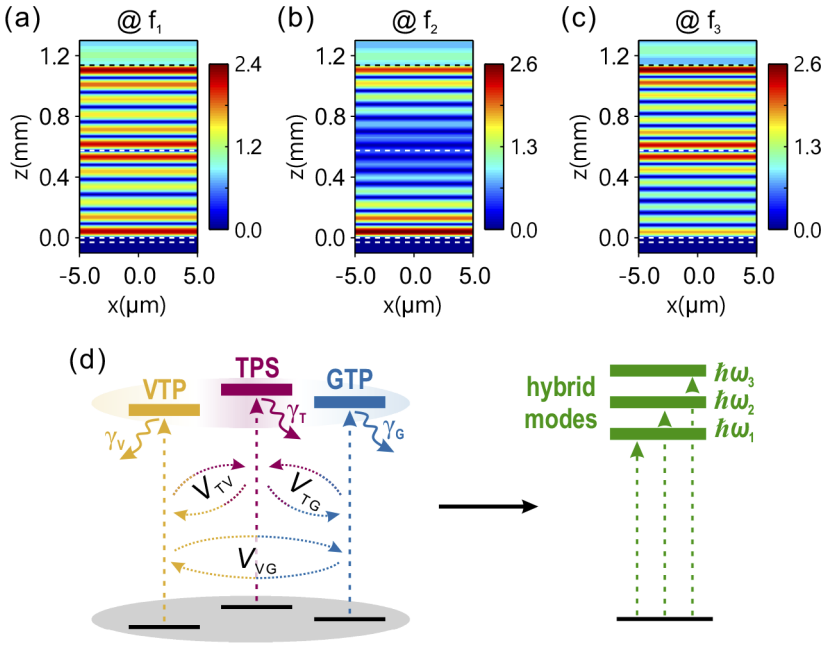

Fig. 4. (a)-(c) The electric field distributions at the frequencies of the peaks P_1-P_3, respectively. The dashed lines indicate the boundaries between the structures. (d) Schematic of the strong coupling process leading to the three perfect absorption peaks.

The strong coupling process here can be described by the coupled oscillator model as [52]

$$\begin{pmatrix} E_T - i\hbar\gamma_T & V_{TV} & V_{TG} \\ V_{TV} & E_V - i\hbar\gamma_V & V_{VG} \\ V_{TG} & V_{VG} & E_G - i\hbar\gamma_G \end{pmatrix} \begin{pmatrix} \alpha_T \\ \alpha_V \\ \alpha_G \end{pmatrix} = E \begin{pmatrix} \alpha_T \\ \alpha_V \\ \alpha_G \end{pmatrix}, \tag{5}$$

where E_T, E_V and E_G are the energies of the TPS, VTP and GTP, γ_T, γ_V and γ_G are the half-width at half-maximum related to the damping rates of the TPS, VTP and GTP, V_{TV}, V_{TG} and V_{VG} are the interaction potential between the two modes, E is the energy of the generated hybrid mode, $|\alpha_T|^2$, $|\alpha_V|^2$ and $|\alpha_G|^2$ represent the mixing fractions of the TPS, VTP and GTP components in the hybrid mode, respectively. Here, the values of E_T, E_V, E_G, γ_T, γ_V, γ_G and E can be obtained from the simulation results, and then those of V_{TV}, V_{TG}, V_{VG}, $|\alpha_T|$, $|\alpha_V|$ and $|\alpha_G|$ can be

Optics EXPRESS

calculated based on Eq. (5). As a result, the interaction potentials in the ON state are $V_{TV} = 0.025$ THz, $V_{TG} = 0.003$ THz, and $V_{VG} = 0.025$ THz. Those in the VON state are $V_{TV} = 0.028$ THz, and $V_{TG} = V_{VG} = 0$. Those in the GON state are $V_{TG} = 0.023$ THz, and $V_{TV} = V_{VG} = 0$.

3. Modulations and discussions

In the insulator-metal phase transition process of VO_2, the conductivity σ_{VO2} varies from 10 S/m to 2×10^5 S/m, which affects the strength and damping rate of the VTP, as indicated by the dashed lines in Fig. 5. As displayed in Fig. 5(a) for $E_F = 0$, no absorption changes into single-band absorption when σ_{VO2} increases to 2×10^3 S/m from the OFF state. The absorption of the TPS is enhanced because of the weak coupling between VTP and TPS. The VTP-TPS coupling strength increases with the σ_{VO2}, which turns into strong coupling regime when σ_{VO2} exceeds 6×10^3 S/m, leading to the switch from single-band to dual-band absorption. As a result, the OFF state finally turns into VON state with two absorption bands, as shown in Fig. 5(a). The detune between the frequencies of TPS and VTP leads to the asymmetric profile of the two peaks in the VON state, even though both VTP and TPS in Fig. 3(a) behave symmetric profiles. Similarly, if the Fermi level of graphene is 0.7 eV, it switches from the GON state to ON state as the VO_2 transits from insulator to metal phase. The absorptions of the two bands in the GON state are enhanced as σ_{VO2} increasing to 2×10^3 S/m, due to the weak coupling between VTP and the other two modes. When σ_{VO2} increases over 6×10^3 S/m, the two absorption bands gradually split into three bands because of the strong coupling. Therefore, σ_{VO2} has a great impact on the coupling strength, result in the affection on the absorption strength and the band number.

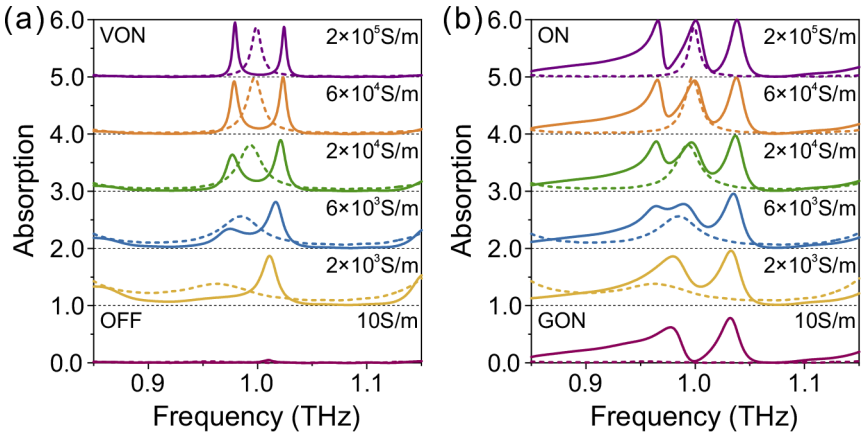

Fig. 5. Tuning σ_{VO2}, the absorption spectra with offset when (a) $E_F = 0$ eV and (b) $E_F = 0.7$ eV, with those of the V/PC_1 for comparison (dashed lines).

Besides, the Fermi level of graphene offers another means to control the multi-band absorption. Increasing the E_F, the absorption spectra in the ON state are shown in Fig. 6(a). The working frequencies of the three absorption bands blue-shift with the Fermi level. The dispersion properties are inherited from the GTP, indicated by the blue dashed line. Seen from Fig. 6(b), the three peaks narrow down with the E_F as well, due to the decrease of the GTP bandwidth. Employing Eq. (5), the frequencies of the absorption bands are calculated, as depicted by the black dashed lines, fitting well with the simulation results. Moreover, the mixing fractions of TPS, VTP and GTP in every absorption band are displayed in Figs. 6(c)–6(e). As E_F increasing, the P_1 turns from GTP-like into VTP-like, the P_2 turns from more VTP-like into equal proportion mixing, and the P_3 turns from TPS-like into GTP-like, leading to the deformation of the absorption bands.

Optics EXPRESS

Accordingly, changing the Fermi level of graphene, both the absorption frequencies and the bandwidths of the absorption bands can be modified.

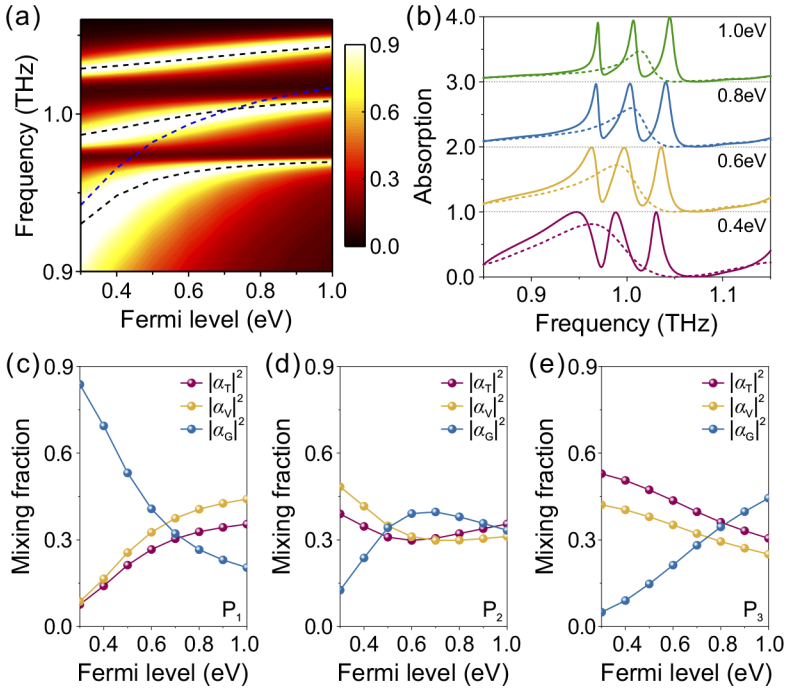

Fig. 6. (a) The variation of the absorption spectra related to the Fermi level E_F. The black dashed lines show the fitting results and the blue dashed line indicates the GTP mode. (b) The absorption spectra with offset for different E_F, with those of the PC_2/graphene for comparison (dashed lines). (c)-(e) The mixing fractions of TPS ($|\alpha_T|^2$), VTP ($|\alpha_V|^2$) and GTP ($|\alpha_G|^2$) in P_1-P_3, respectively.

Different from the σ_{VO2} and E_F, which control the absorption bands via influencing the VTP and GTP, respectively, the incident angle can simutaneously affect all the TPS, VTP, and GTP. Increasing the incident angle, the absorption spectra in the ON state under TM illumination are shown in Fig. 7(a). The three absorption peaks turns to higher frequencies altogether, with almost the same dispersion. Such a dispersion property can find explanations from Fig. 7(b). The three single modes, TPS, VTP and GTP, all shift to higher frequencies, with almost the same dispersion as well. Consequently, the coupling strengths V_{TV}, V_{TG} and V_{VG} remain nearly unchanged as the incident angle varies, leading to the similar dispersion properties of the three absorption peaks. As this planer multilayer structure is isotropic in *x*-*y* plane, similar dispersion would occur under TE illumination. The three absorption peaks keep above 0.95 and distinguishable to each other even for the incident angle as large as 60°, with the frequencies varied about 0.11THz. Hence, this absorber is sensitive to the incident angle in a wide angle range, which helps it to find applications in sensors.

Apart from the active modulation elements, there is also an important passive parameter that impacts the multiple absorption peaks by influencing the TPS, VTP and GTP in the meanwhile, which is the pair number of the alternative multilayers in the PC_1 and PC_2. As shown in Figs. 8(a) and 8(b), the splitting between the two adjacent absorption peaks decreases with the pair number, for all the ON, VON and GON states, accompanied by the decrease of the damping rates of TPS, VTP and GTP in Figs. 8(c) and 8(d). Moreover, the absorption of the VTP gradually vanishes while the pair number increases to 13. As a result, the peak number in the ON state reduces

Optics EXPRESS

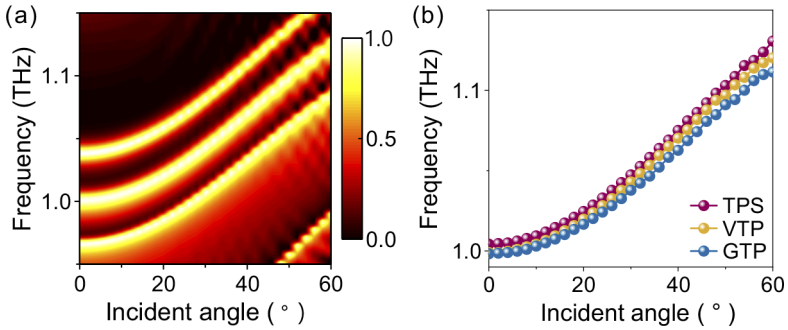

Fig. 7. (a) The variation of the absorption spectra related to the incident angle. (b) The frequencies of the TPS, VTP and GTP modes for different incident angles.

to two and that in the VON state reduces to one. Define the damping factors of the adjacent absorption peaks in the ON state as $\Gamma_{ij} = (\gamma_i + \gamma_j)/2$, and the splitting frequencies between them as $\Delta f_{ij} = f_j - f_i$, in which (i, j) is (1, 2) or (2, 3) for P_1-P_3. Thereby, the strong coupling regime can be expressed as $\Gamma_{ij} < \Delta f_{ij}$, where the splitting is larger than the damping. Otherwise, it enters the

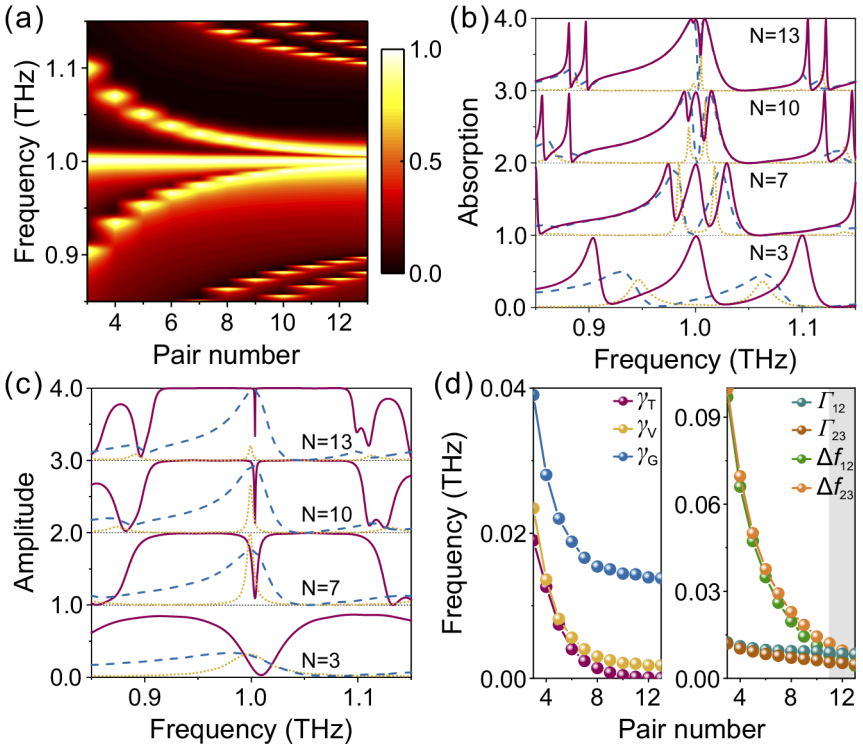

Fig. 8. (a) The absorption spectra in the ON state related to the pair number in the PC_1 and PC_2. (b) The absorption spectra with offset in the ON (solid lines), VON (dotted lines) and GON (dashed lines) states. (c) The reflection spectra with offset for the PC_1/PC_2 (solid lines), and the absorption spectra of the V/PC_1 (dotted lines) and PC_2/G (dashed lines). (d) The damping rates of the TPS (γ_T), VTP (γ_V) and GTP (γ_G), the damping factors of the adjacent absorption peaks (Γ_{12} and Γ_{23}), and the frequency differences between the adjacent peaks (Δf_{12} and Δf_{23}).

Optics EXPRESS

weak coupling regime, where the neighbouring modes superimpose into one mode. As displayed in Fig. 8(d), the strong coupling enters to weak coupling as the pair number increase to above 10, with the three absorption peaks gradually reducing to two and even one. Therefore, the splitting of the three absorption peaks can be decided by the pair number, which is in the range from 3 to 10 to keep every peak distinguishable.

As the pair number increasing, more perfect absorption peaks appear in both sides of the multi-peaks we are interested. Thus, we expand the frequency range in simulation to explore the existence of the other absorptions for the pair number of 6. As shown in Fig. 9(a), multiple absorption peaks appear besides the peaks around 1THz. There are altogether 10 peaks whose absorptions are above 0.9 in the range between 0.83THz and 1.55THz, and 16 peaks above 0.8 in the range from 0.69THz to 1.86THz. At the frequencies around 1THz and 3THz, hybrid strong couplings among TPS, VTP and GTP occur, leading to the three splitting absorption peaks. At the frequencies around 2THz, weak coupling results in the enhancement of the original low absorptions in the $VO_2/PC_1/PC_2$ structure, without frequency shift and mode splitting. Apart from these, the other absorption peaks decrease for the frequencies away from 1THz.

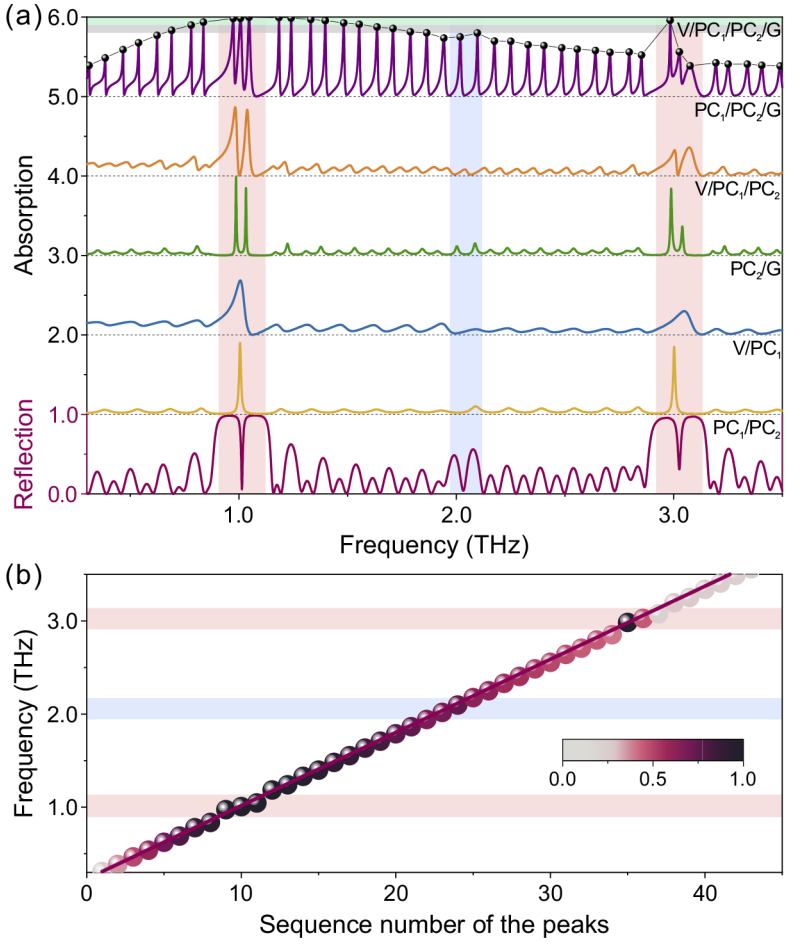

Fig. 9. (a) The reflection/absorption spectra with offset for different structures in the large frequency range, where the green and gray shadows indicate the absorptions above 0.9 and 0.8, the blue and red shadows indicate the weak and strong couplings, respectively. (b) The frequencies and amplitudes of the absorption peaks, with the fitted results (solid line).

Optics EXPRESS

Extracting the frequencies and absorptance of the peaks, the results are displayed in Fig. 9(b). Except the peaks around 1THz, 2THz and 3THz that comes from strong and weak couplings, the frequency differences between the adjacent absorption peaks are almost the same, because they all come from the standing waves, which are absence in the other structures in Fig. 9(a). Thus, the frequencies of the absorption peaks should following

$$f = \frac{mc}{2\Sigma(n_i d_i)}, \tag{6}$$

where $\Sigma(n_i d_i)$ is the optical distance between graphene and VO_2, m is a positive integer, and c is the light speed in vacuum. The peak frequencies calculated via Eq. (6) are shown by the solid line in Fig. 9(b), where the first peak is related to $m = 4$ and the gradient is about 78.6 GHz, fitting well with the simulation results. Therefore, this system can actually support multiple absorption peaks due to different mechanisms, including strong coupling, weak coupling and standing wave.

4. Summary

In summary, we propose a multi-band perfect absorber with multiple active control means, whose absorption peaks around 1THz come from the hybrid strong coupling among the TPS, VTP and GTP. The properties of the absorber can be actively tuned by the σ_{VO2} and E_F. The σ_{VO2} mainly affects the absorption band number, while the E_F mainly impacts the frequencies of the absorption bands. Consequently, the absorber can turn from no absorption to single-band, dual-band and even multi-band absorption, with the absorption frequencies controllable. Besides, the absorber is sensitive to the incident angle and keeps high absorptions in a wide angle range. Apart from the active modulation, the pair number of the multilayers affect the coupling strength as well, resulting in the variation of the splitting frequencies between the adjacent absorption peaks. Moreover, the multilayered system also supports a lot of absorption peaks in the large frequency range, which result from the standing wave. Such an active multi-band absorber with multiple modulation methods may achieve potential applications in active integrated terahertz devices, such as switches, filters, detectors and sensors.

Funding. National Natural Science Foundation of China (11804178); Natural Science Foundation of Shandong Province (ZR2018BA027); National Laboratory of Solid State Microstructures, Nanjing University (M34009).

Disclosures. The authors declare no conflicts of interest.

Data availability. Data underlying the results presented in this paper are not publicly available at this time but may be obtained from the authors upon reasonable request.

References

1. P. U. Jepsen, D. G. Cooke, and M. Koch, "Terahertz spectroscopy and imaging - Modern techniques and applications," Laser Photonics Rev. **5**(1), 124–166 (2011).
2. S. Koenig, D. Lopez-Diaz, J. Antes, F. Boes, R. Henneberger, A. Leuther, A. Tessmann, R. Schmogrow, D. Hillerkuss, R. Palmer, T. Zwick, C. Koos, W. Freude, O. Ambacher, J. Leuthold, and I. Kallfass, "Wireless sub-THz communication system with high data rate," Nat. Photonics **7**(12), 977–981 (2013).
3. J. J. Liu, L. L. Fan, J. F. Ku, and L. L. Mao, "Absorber: a novel terahertz sensor in the application of substance identification," Opt. Quant. Electron. **48**(2), 80 (2016).
4. S. Savo, D. Shrekenhamer, and W. J. Padilla, "Liquid Crystal Metamaterial Absorber Spatial Light Modulator for THz Applications," Adv. Opt. Mater. **2**(3), 275–279 (2014).
5. K. Iwaszczuk, A. C. Strikwerda, K. B. Fan, X. Zhang, R. D. Averitt, and P. U. Jepsen, "Flexible metamaterial absorbers for stealth applications at terahertz frequencies," Opt. Express **20**(1), 635–643 (2012).
6. N. I. Landy, C. M. Bingham, T. Tyler, N. Jokerst, D. R. Smith, and W. J. Padilla, "Design, theory, and measurement of a polarization-insensitive absorber for terahertz imaging," Phys. Rev. B **79**(12), 125104 (2009).
7. N. I. Landy, S. Sajuyigbe, J. J. Mock, D. R. Smith, and W. J. Padilla, "Perfect metamaterial absorber," Phys. Rev. Lett. **100**(20), 207402 (2008).
8. M. P. Hokmabadi, D. S. Wilbert, P. Kung, and S. M. Kim, "Design and analysis of perfect terahertz metamaterial absorber by a novel dynamic circuit model," Opt. Express **21**(14), 16455–16465 (2013).
9. H. Tao, C. M. Bingham, A. C. Strikwerda, D. Pilon, D. Shrekenhamer, N. I. Landy, K. Fan, X. Zhang, W. J. Padilla, and R. D. Averitt, "Highly flexible wide angle of incidence terahertz metamaterial absorber: Design, fabrication, and characterization," Phys. Rev. B **78**(24), 241103 (2008).

Optics EXPRESS

10. M. Wu, X. Zhao, J. Zhang, J. Schalch, G. Duan, K. Cremin, R. D. Averitt, and X. Zhang, "A three-dimensional all-metal terahertz metamaterial perfect absorber," Appl. Phys. Lett. **111**(5), 051101 (2017).
11. L. Huang, D. R. Chowdhury, S. Ramani, M. T. Reiten, S. N. Luo, A. J. Taylor, and H. T. Chen, "Experimental demonstration of terahertz metamaterial absorbers with a broad and flat high absorption band," Opt. Lett. **37**(2), 154–156 (2012).
12. S. Yin, J. Zhu, W. Xu, W. Jiang, J. Yuan, G. Yin, L. Xie, Y. Ying, and Y. Ma, "High-performance terahertz wave absorbers made of silicon-based metamaterials," Appl. Phys. Lett. **107**(7), 073903 (2015).
13. Y. Z. Cheng, W. Withayachumnankul, A. Upadhyay, D. Headland, Y. Nie, R. Z. Gong, M. Bhaskaran, S. Sriram, and D. Abbott, "Ultrabroadband Plasmonic Absorber for Terahertz Waves," Adv. Opt. Mater. **3**(3), 376–380 (2015).
14. X. Cheng, R. Huang, J. Xu, and X. Xu, "Broadband Terahertz Near-Perfect Absorbers," ACS Appl. Mater. Inter. **12**(29), 33352–33360 (2020).
15. Q. Y. Wen, H. W. Zhang, Y. S. Xie, Q. H. Yang, and Y. L. Liu, "Dual band terahertz metamaterial absorber: Design, fabrication, and characterization," Appl. Phys. Lett. **95**(24), 241111 (2009).
16. Y. Ma, Q. Chen, J. Grant, S. C. Saha, A. Khalid, and D. R. Cumming, "A terahertz polarization insensitive dual band metamaterial absorber," Opt. Lett. **36**(6), 945–947 (2011).
17. S. Hussain, J. Min Woo, and J. H. Jang, "Dual-band terahertz metamaterials based on nested split ring resonators," Appl. Phys. Lett. **101**(9), 091103 (2012).
18. M. Kang, H. Zhang, X. Zhang, Q. Yang, W. Zhang, and J. Han, "Interferometric Control of Dual-Band Terahertz Perfect Absorption Using a Designed Metasurface," Phys. Rev. Appl. **9**(5), 054018 (2018).
19. M. T. Reiten, D. Roy Chowdhury, J. Zhou, A. J. Taylor, J. F. O'Hara, and A. K. Azad, "Resonance tuning behavior in closely spaced inhomogeneous bilayer metamaterials," Appl. Phys. Lett. **98**(13), 131105 (2011).
20. X. Shen, Y. Yang, Y. Zang, J. Gu, J. Han, W. Zhang, and T. Jun Cui, "Triple-band terahertz metamaterial absorber: Design, experiment, and physical interpretation," Appl. Phys. Lett. **101**(15), 154102 (2012).
21. Y. Wang, Z. Cui, D. Zhu, X. Wang, S. Chen, and P. Nie, "Multiband terahertz absorber and selective sensing performance," Opt. Express **27**(10), 14133–14143 (2019).
22. L. Yue, Y. Wang, Z. Cui, X. Zhang, Y. Zhu, X. Zhang, S. Chen, X. Wang, and K. Zhang, "Multi-band terahertz resonant absorption based on an all-dielectric grating metasurface for chlorpyrifos sensing," Opt. Express **29**(9), 13563–13575 (2021).
23. X. Wang, X. Jiang, Q. You, J. Guo, X. Dai, and Y. Xiang, "Tunable and multichannel terahertz perfect absorber due to Tamm surface plasmons with graphene," Photonics Res. **5**(6), 536–542 (2017).
24. J. Hu, E. Yao, W. Xie, W. Liu, D. Li, Y. Lu, and Q. Zhan, "Strong longitudinal coupling of Tamm plasmon polaritons in graphene/DBR/Ag hybrid structure," Opt. Express **27**(13), 18642–18652 (2019).
25. K. Zhang, Y. Liu, F. Xia, S. Li, and W. Kong, "Tuning of the polariton modes induced by longitudinal strong coupling in the graphene hybridized DBR cavity," Opt. Lett. **45**(13), 3669–3672 (2020).
26. H. R. Seren, G. R. Keiser, L. Cao, J. Zhang, A. C. Strikwerda, K. Fan, G. D. Metcalfe, M. Wraback, X. Zhang, and R. D. Averitt, "Optically Modulated Multiband Terahertz Perfect Absorber," Adv. Opt. Mater. **2**(12), 1221–1226 (2014).
27. G. Isić, B. Vasić, D. C. Zografopoulos, R. Beccherelli, and R. Gajić, "Electrically Tunable Critically Coupled Terahertz Metamaterial Absorber Based on Nematic Liquid Crystals," Phys. Rev. Appl. **3**(6), 064007 (2015).
28. R. Wang, L. Li, J. Liu, F. Yan, F. Tian, H. Tian, J. Zhang, and W. Sun, "Triple-band tunable perfect terahertz metamaterial absorber with liquid crystal," Opt. Express **25**(26), 32280–32289 (2017).
29. Z. Wang and Y. Hou, "Ultra-multiband absorption enhancement of graphene in a metal-dielectric-graphene sandwich structure covering terahertz to mid-infrared regime," Opt. Express **25**(16), 19185–19194 (2017).
30. L. Ye, Y. Chen, G. Cai, N. Liu, J. Zhu, Z. Song, and Q. H. Liu, "Broadband absorber with periodically sinusoidally-patterned graphene layer in terahertz range," Opt. Express **25**(10), 11223–11232 (2017).
31. L. Qi, C. Liu, and S. M. Ali Shah, "A broad dual-band switchable graphene-based terahertz metamaterial absorber," Carbon **153**, 179–188 (2019).
32. Y. Cai, Y. Guo, Y. Zhou, X. Huang, G. Yang, and J. Zhu, "Tunable dual-band terahertz absorber with all-dielectric configuration based on graphene," Opt. Express **28**(21), 31524–31534 (2020).
33. H. Meng, X. Shang, X. Xue, K. Tang, S. Xia, X. Zhai, Z. Liu, J. Chen, H. Li, and L. Wang, "Bidirectional and dynamically tunable THz absorber with Dirac semimetal," Opt. Express **27**(21), 31062–31074 (2019).
34. Z. Song, K. Wang, J. Li, and Q. H. Liu, "Broadband tunable terahertz absorber based on vanadium dioxide metamaterials," Opt. Express **26**(6), 7148–7154 (2018).
35. J. Huang, J. Li, Y. Yang, J. Li, J. Li, Y. Zhang, and J. Yao, "Broadband terahertz absorber with a flexible, reconfigurable performance based on hybrid-patterned vanadium dioxide metasurfaces," Opt. Express **28**(12), 17832–17840 (2020).
36. T. Lv, G. Dong, C. Qin, J. Qu, B. Lv, W. Li, Z. Zhu, Y. Li, C. Guan, and J. Shi, "Switchable dual-band to broadband terahertz metamaterial absorber incorporating a VO_2 phase transition," Opt. Express **29**(4), 5437–5447 (2021).
37. H. Xiong, Y. Peng, F. Yang, Z. Yang, and Z. Wang, "Bi-tunable terahertz absorber based on strontium titanate and Dirac semimetal," Opt. Express **28**(10), 15744–15752 (2020).
38. H. Zhu, Y. Zhang, L. Ye, Y. Li, Y. Xu, and R. Xu, "Switchable and tunable terahertz metamaterial absorber with broadband and multi-band absorption," Opt. Express **28**(26), 38626–38637 (2020).
39. X. Gao, Z. Zhu, J. Yuan, and L. Jiang, "Tunable and multifunctional terahertz devices based on one-dimensional anisotropic photonic crystals containing graphene and phase-change material," Opt. Express **29**(9), 13314–13330 (2021).

Optics EXPRESS

40. M. Kaliteevski, I. Iorsh, S. Brand, R. A. Abram, J. M. Chamberlain, A. V. Kavokin, and I. A. Shelykh, "Tamm plasmon-polaritons: Possible electromagnetic states at the interface of a metal and a dielectric Bragg mirror," Phys. Rev. B **76**(16), 165415 (2007).
41. I. Tamm, "Über eine mögliche Art der Elektronenbindung an Kristalloberflächen," Z," Z. Physik **76**(11-12), 849–850 (1932).
42. M. Xiao, Z. Q. Zhang, and C. T. Chan, "Surface Impedance and Bulk Band Geometric Phases in One-Dimensional Systems," Phys. Rev. X **4**(2), 021017 (2014).
43. W. Tan, Y. Sun, H. Chen, and S. Q. Shen, "Photonic simulation of topological excitations in metamaterials," Sci. Rep. **4**(1), 3842 (2015).
44. A. Podzorov and G. Gallot, "Low-loss polymers for terahertz applications," Appl. Opt. **47**(18), 3254–3257 (2008).
45. M. Naftaly and R. E. Miles, "Terahertz time-domain spectroscopy: A new tool for the study of glasses in the far infrared," J. Non-Cryst. Solids **351**(40-42), 3341–3346 (2005).
46. F. H. Koppens, D. E. Chang, and F. J. Garcia de Abajo, "Graphene plasmonics: a platform for strong light-matter interactions," Nano Lett. **11**(8), 3370–3377 (2011).
47. A. Vakil and N. Engheta, "Transformation optics using graphene," Science **332**(6035), 1291–1294 (2011).
48. S. Wang, L. Kang, and D. H. Werner, "Hybrid Resonators and Highly Tunable Terahertz Metamaterials Enabled by Vanadium Dioxide (VO_2)," Sci. Rep. **7**(1), 4326 (2017).
49. J. W. Han, S. Y. Hamh, T. H. Kim, K. S. Lee, N. E. Yu, D. K. Ko, and J. S. Lee, "Extraction of optical constants using multiple reflections in the terahertz emitter-sample hybrid structure," Opt. Lett. **39**(19), 5531–5534 (2014).
50. P. U. Jepsen, B. M. Fischer, A. Thoman, H. Helm, J. Y. Suh, R. Lopez, and R. F. Haglund, "Metal-insulator phase transition in a VO_2 thin film observed with terahertz spectroscopy," Phys. Rev. B **74**(20), 205103 (2006).
51. Q. Y. Wen, H. W. Zhang, Q. H. Yang, Y. S. Xie, K. Chen, and Y. L. Liu, "Terahertz metamaterials with VO_2 cut-wires for thermal tunability," Appl. Phys. Lett. **97**(2), 021111 (2010).
52. A. Christ, S. G. Tikhodeev, N. A. Gippius, J. Kuhl, and H. Giessen, "Waveguide-plasmon polaritons: strong coupling of photonic and electronic resonances in a metallic photonic crystal slab," Phys. Rev. Lett. **91**(18), 183901 (2003).